Cleavage Fracture in Ferritic Steel Weld: Characterization of second phase particles

Cleavage Fracture in a Ferritic Steel Weld: Characterization of Second Phase Particles

S. Schilling, Materials Performance Centre, University of Manchester, Manchester, UK;
N. Chapeau, ENSCL, Villeneuve d'Ascq, France
A. P. Jivkov, Modelling and Simulation Centre, University of Manchester, Manchester, UK;
E. Keim, AREVA NP GmbH, Erlangen, Germany
S. R. Ortner, NNL, Sellafield, UK;
M. G. Burke, Materials Performance Centre, University of Manchester, Manchester, UK;

Abstract

Cleavage fracture can initiate by the cracking of second phase particles in metals. Understanding the size distribution, morphologies and compositions of initiating particles for a particular material is key to successful micromechanical modelling of cleavage. The second phase particles responsible for the fracture initiation in P141 CAC-S7, a reactor pressure vessel (RPV) weld metal from the EU-funded PERFORM 60 Multiscale Modelling Programme, have been identified and characterised in order to aid the development of a fracture model.

Fractographic characterisation of CVN samples tested in the lower shelf region of the transition temperature curve was performed to identify cleavage initiation sites. The general microstructural characterisation of the material including fracture-initiating particles (inclusions) involved optical, laser scanning confocal and scanning electron microscopy combined with energy dispersive x-ray (EDX) microanalysis. The project used novel TEM-type specimens for microstructural analysis. The size and distribution of the inclusions present within the material were evaluated using image analysis techniques.

The inclusions present throughout the weld were spherical, and predominantly manganese alumino-silicate with traces of titanium and magnesium. The size distribution of the inclusions responsible for the initiation of the cracks is presented together with comprehensive statistical analysis as well as how these results will be used in predictive modelling of cleavage fracture as part of the future work of PEFORM 60.

Keyword: Cleavage fracture, second phase particles, size distribution, multiscale modelling

Introduction

Understanding the fracture behaviour of the steels and welds used in reactor pressure vessels (RPVs) of pressurized water reactors (PWRs) is critical for ensuring the safe operation of these reactors over their intended design lifetime and for periods of extended license operations. For the RPV to be resistant to catastrophic fracture, the ferritic/bainitic steels from which the vessels are made and their weldments must be resistant to brittle fracture during normal and potential faulted operating conditions. In addition to withstanding normal operating pressure-driven stresses at temperature, the material of the vessel must be able to withstand the transient conditions of heat-up and cool-down as well as the off-normal conditions that might prevail during accident conditions. The conditions most critical to vessel integrity are those that would occur during pressurized thermal shock, i.e. under pressurized conditions and due to the ingress of cold cooling water from outside the primary cooling circuit, the vessel tensile stresses would be augmented by rapid cooling of the internal surface region while at the same time the material properties are driven into a lower temperature regime where brittle facture may occur.

While pressure vessel steels are initially selected to provide substantial margin to accommodate pressurized thermal shock conditions, over time as a result of thermal and more particularly neutron irradiation exposures, these materials' structures have been found to degrade and their resistance to brittle fracture has been observed to decrease. Specifically, neutron irradiation causes the displacement of atoms in the steel, enhancing diffusion, and promoting the formation of solute-clusters and defects in the microstructure. These features then act as ultrafine scale obstacles to mobile dislocations to harden the microstructure. Hardening alone can increase the tendency to brittle fracture, and it is generally assumed that radiation does not otherwise alter the fracture initiating process in the subject ferritic-bainitic steels. In PWR RPV steels the increased tendency towards brittle fracture is manifested by an increase in the temperature of transition between brittle and ductile behaviours, often measure by the temperature at which the absorbed energy of a Charpy impact specimen of the material will increase above 41 Joules. Changes in the behaviour of exposed materials are conveniently characterised by a difference between the transition temperature measured for the exposed material and the corresponding transition temperature measure for the same material prior to exposure. This change in fracture transition temperature signified by ΔDBTT or ΔT_{41J} is often employed to characterize the extent of embrittlement as a function of vessel exposures and plant aging

As plants age the fracture transition temperature for the vessel material is driven higher and the ΔDBTT or ΔT_{41J} increase. The greatest increase and the most relevant region for vessel performance occur in the region of maximum neutron fluence. This region is known as the vessel "beltline". The fracture properties and the potential change in ductile to brittle transition temperature for the materials and welds used in the beltline are therefore of critical concern in ensuring vessel integrity. In practice vessel embrittlement is monitored via surveillance capsule programs and tracking and trending of hardening and embrittlement as functions of material's chemistry and fluence are conducted to ensure continuing vessel safety. Because the RPV cannot be replaced, ensuring that high levels of resistance to fracture, represented by the exposed materials' fracture toughness is crucial to demonstrating the ability to continue to operate the vessel safely.

To underpin the empirical correlations between material chemistry and fluence and hardening and embrittlement, it important to understand the mechanism by which hardening is induced and by which cleavage at increasing temperatures is promoted. Identifying the microstructural features associated with cleavage can help provide this understanding. Because brittle fracture can be induced in the ferritic-bainitic steels and welds by control of the fracture temperature it is not necessary to employ irradiated materials to study the process; non-irradiated steels fractured at low temperatures can provide the relevant

feature-containing specimens required to study the effect of microstructure on the initiation of brittle facture. In this investigation, non-irradiated RPV welds in the form of pre-cracked Charpy V-notch (CVN) samples were fractured under conditions conducive to brittle fracture. Detailed microstructural characterisation of the material was correlated with brittle fracture features and the tendency of brittle fracture as represented by complete Charpy curves and the extracted fracture transition temperatures. The purpose of this work is to establish a mechanistic basis for the experimentally-measured data to be incorporated into a general cleavage fracture model.

Statistical models of fracture and influence of second phase particles

The cleavage fracture of RPV steels is considered to involve a number of stages:

1. Yield (to distribute the load onto the second phase particles);
2. Particle cracking (to produce a sharp microcrack);
3. Microcrack extension into the ferrite matrix despite hindrance from plasticity.

The last stage is sometimes separated into

3a. Microcrack extension into the first grain;

3b. Microcrack extension past the first set of grain boundaries.

All stages must be achieved if cleavage is to occur.

According to the early analysis of Wallin, Saario and Torronen, stage 2 can be modelled as the result of fibre loading on the particles by a ductile matrix [1]. This leads to a particle size-dependence for Stage 2. A more recent model by Laukkanen and Wallin [2] utilises a more general particle loading concept, but predicts a similar particle size dependence for the probability of particle cracking. Another by Jivkov also predicts size dependence for particle cracking [3]. Several models deal with the Stage 3 in the cleavage process. Whether the microcrack is expected to extend under a Griffith-type formulation [4, 5, 6, 7, 8, 9], as a result of the failure of dislocation shielding and blunting [10, 11], the necessary condition incorporate an influence of particle size. It is, therefore, necessary to identify the types of particle initiating fracture and their size distribution if any of these models are to be applied meaningfully to the description of fracture in particular steel.

Experimental procedure

An RPV weld metal, P141 CAC-S7, was provided in the form of fractured Charpy V-notch specimens by Areva NP Gmbh for the PERFORM 60. This material is a German S3NiMo1/OP41 weld.

Fractographic characterisation was performed at the National Nuclear Laboratory using a JEOL JSM-6480LV SEM operated at 20 kV, which was equipped with an Oxford Instruments energy-dispersive X-ray (EDX) detector and INCA analysis system.

Material for microstructural characterisation was obtained by slicing three 1 cm square sections 0.7 mm in thickness from the fractured sample beneath the fracture surface. The slices were mechanically thinned to a final thickness of approximately 100 µm. Next, 3 mm diameter discs were punched from the slices. The disc samples were subsequently electropolished using a Struers Tenupol 5 twin jet polishing unit in an electrolyte of 80% CH_3OH – 20% ClO_4 at -35C and 25 V. The use of this electrolyte resulted in a lightly electro-etched specimen surface, which was amenable for subsequent characterisation using light

optical microscopy (LOM) and scanning electron microscopy (SEM). The general microstructural analysis was performed using a Zeiss EVO 50 Scanning Electron Microscope operated at 20 kV and equipped with an Oxford Instruments EDX spectrometer and an INCA analysis system, and an FEI Sirion Field Emission Gun (FEG) SEM. To complement the conventional LOM examination, an Olympus LEXT OLS4000 Laser Scanning Confocal microscope was used to obtain enhanced optical microstructures.

Results and Discussion

Fractographic characterisation of the pre-cracked CVN samples tested near the lower shelf revealed a classic brittle cleavage morphology, as shown in Figure 1. These secondary electron images show the classic 'river' markings on the cleavage facets and evidence of the fracture-initiating features. EDX analysis showed that the cracked particle at the initiation site, like the particles found at the initiation sites in 7 other samples was high in Mn, Al, Si and O, with traces of Ti. The particles were identified as manganese alumino-silicate inclusions from the welding process. The diameters of the fracture-initiating inclusions ranged from 0.4-1.8µm (width) with aspect ratios (length/width) between 1 and 1.7 (average 1.3).

Evaluation of the weld microstructure by Light Optical Microscopy (LOM) of electropolished/electroetched TEM-type specimens revealed an acicular ferritic microstructure with evidence of carbide precipitation. Figure 2 contains typical microstructures observed in the weldment. The weld microstructure consisted of fine ferrite grains as well as a fine acicular structure. Due to the nature of the TEM specimen (concave polished surface resulting from the electropolishing process), conventional LOM focussing can be difficult because the region around the point in focus is also excited and this light does not come to a focal point on the camera, which gives blurry-out-of-focus images in the case of non-planar samples. For Laser Scanning Confocal Microscopy, a pinhole that passes only light that comes from the sample focal plan is acquired. A laser scans across the sample and the intensity at each plane in the z-dimension (height) is recorded as opposed to acquiring a single image at one focal plane over the entire sample. The series of confocal images are reconstructed to produce a single in-focus image [12]. This technique produces clearer optical micrographs (see Figure 4) of the microstructure of grain, with the inclusions and carbides appearing as black dots.

SEM characterisation of the same specimens yielded clear images of the acicular ferritic microstructure contining both intergranular and intragranular carbides. Typical structures observed in the weld are presented in the secondary electron (SE) images of Figure 5 and Figure 6. Figure 5 shows very fine acicular ferritic regions with fine intragranular and intergranular carbides. These carbides were not uniformly distributed in the specimens. The fractographic analyses demonstrated that these fine carbides were not associated with cleavage fracture and were therefore not evaluated further. The SE images of Figure 7 show relatively homogeneously distributed spheroidal particles observed in the "electropolished" samples. These features were identified as Mn-Al-Si-O inclusions, which also contained lower levels of Ti and Mg (see Figure 8).

Statistical analysis

117 SE images (magnification of 2000x) were analysed to determine the relevant inclusion size distributions. Image processing was performed to produce binary images for analysis, and commercial software (Image J) was used to assess the average diameter, "length", "width", particle area, equivalent diameter, perimeter and Feret diameter, and nearest-neighbor distance. Approximately 2700 particles were analysed. These results are summarised in Table 1. Since the electropolishing process caused the inclusions to sit proud

of the polished surface, the particle diameters seen in the images are taken to be actual particle diameter rather than merely the diameter if a random section through each particle.

The number of inclusions analysed (2700) was considered adequate for this type of evaluation, and represents nearly double the number compared to a previous fracture study [13]. Thus, it appears that a reasonably sufficient sampling so that the results are a good approximation of the actual inclusion distribution within the weld microstructure. It is noted that the images were obtained in the zones where there were at least 4 inclusions in the field of view. However, it should be noted that there were fields-of-view in the weld where no inclusions were present. Also, with the presence of holes on the “electropolished” samples can indicate possible fine-scale pitting due to the electrolytic conditions or may indicate sites where inclusions were removed during this same process. It is recognized that this could have a minor effect on the inclusion area fraction and average size. The average values for the stereological measurements are presented in Table 2.

Analyses confirmed that the inclusions were generally round with an average circularity of 0.93. The values of accuracy presented in **Error! Reference source not found.** have been calculated by taking into account the contribution of both the measure repeatability of ImageJ and the limitation due to image resolution. The difference between this average and that seen on the fracture surface is probably due to the much smaller number of fracture initiating particles measured.

The inclusion size distribution is presented in Figure 9. It was noted that the size distribution, which was verified with the other stereological measurements, did not follow a normal distribution, and that there was a broad size spread in the tail of the distribution. This distribution has been used to verify if the data can be modelled by a power law, fitting the tail. To fit the histogram with best accuracy possible, the centre of each bins used to make the histograms has been plotted against the number of inclusions contained in each bin. Then a power law of the type

$$K \times \left(\frac{r}{r_0} \right)^{-\alpha} \qquad (4)$$

has been fitted, with r the particle size, r_0 the minimum particle size, K a coefficient and α the shape of the particle size distribution. The power law form often chosen as a first estimate for the description of fracture-initiating particles because fracture is an extreme event. In extreme value statistics, only the tail of the distribution is considered to be significant, and the tails of natural distributions can always be approximated by power laws. The optimising of the relation has been carried out by iterative modifications to the values of K, r_0 and a. The optimised fit is presented on the **Error! Reference source not found.**
The mathematical formula for this fit is

$$f(r) = 405 \times \left(\frac{r}{0.6} \right)^{-3.72} \qquad (5)$$

Although this mathematical form does provide a good fit to the upper tail of the distribution, it does not fit down to the minimum size of inclusion actually observed to initiate fracture (i.e. 0.4μm) thus it does not adequately model all the relevant data. It can be concluded that the power law is not the best function to use for modelling the inclusion distribution tail, and consequently, should not be used in the predictive fracture models.

The cumulative probability function has also been graphically represented. This allows one to determine the probability of finding an inclusion of a size larger than a given size r. The cumulative probability function is estimated by calculating the median rank given by the formula

$$F(i) = \frac{i - 0.3}{n + 0.4} \qquad (6)$$

with (i) from 1 to n, the total number of inclusions. With this formula, the minimal value is not 0 and the maximum probability is not equal to 1 because it is assumed that there are other inclusions. The median rank is then plotted against the size data and as it has been observed that the power law wasn't fitting well on the probability density function, another fit was tried on the representation of the cumulative probability function (Figure 11). It contains more data because this graph is made of raw data, unlike the probability density function which is determined with bins.

The function that has been found to best fit the entire range of sizes is the logistic function given by

$$F(r) = 1 - \frac{1}{1 + (r/r_0)^p} \qquad (7)$$

Where the scale r_0 and the shape p of the cumulative size distribution are depicted in the figure. The derivative of logistic fit gives an analytical expression for the probability density function

$$f(r) = \frac{p}{r} \frac{(r/r_0)^p}{\left[1 + (r/r_0)^p\right]^2} \qquad (8),$$

which can be used in improved models for cleavage fracture based on the full particle size distribution. The next stage in this work will be the incorporation of this inclusion distribution into predictions of fracture using a number of different fracture models within the PERFORM-60 program. The aim will be to determine how well the associated measurements of fracture toughness and the locations of the fracture initiation sites can be predicted by the different models, and to gain insight into the most likely roles played by stress and strain in the cleavage fracture of RPV steels.

Conclusions

By using LOM and SEM-EDX analyses it has been possible to characterise the weld microstructure. This material was acicular ferrite with carbides and spheroidal inclusions. The weld metal contained 2 different types of non-metallic inclusions pertinent for this study, as well as fine carbides. Microstructural analysis revealed that the inclusions were predominantly manganese alumina-silicates that contained titanium and magnesium. The fractographic analyses of pre-cracked CVN specimens demonstrated that the Mn-Al-Si-O inclusions were associated with the nucleation of cleavage fracture. The fine carbides observed in the acicular ferrite weld were not associated with cleavage fracture.

Quantitative stereological data for the inclusions in an RPV weld were successfully generated from the novel TEM-type specimens for use in the development of predictive models for cleavage fracture. The size distribution of the inclusions responsible for the initiation of cleavage cracks was modelled as a mathematical function for use in predictive fracture models.

References

[1] K. Wallin, T. Saario and K. Törrönen, “Fracture Of Brittle Particles In A Ductile Matrix”, Int. J. Fract., 32, 201-209 (1987).

[2] A. Laukkanen and K. Wallin, “Finite Element Analysis Of Continuum Fields For Cleavage Fracture Evaluation” VTT Report BTUO72-051372 (2005).

[3] A.P. Jivkov, P. James, Cleavage modelling with experimental particle size distribution and novel particle failure criterion, Proc. 13th Int Conf Fracture, Paper M10-004, June 16-21, 2013, Beijing, China

[4] A. A. Griffith, “The Phenomena Of Rupture And Flow In Solids”, Phil. Trans. Roy Soc. Lond. A, 221, 163-198 (1920).

[5] E. Orowan, “Fundamentals Of Brittle Behaviour In Metals” in “Fatigue And Fracture Of Metals” Proc. Symp. held MIT 1950. Ed. W.M.Murray, pub. John Wiley, New York pp139-154.

[6] F. M. Beremin, “A Local Criterion For Cleavage Fracture Of A Nuclear Pressure Vessel Steel”, Metall. Trans, 14A, 2277-2287 (1983).

[7] S. R. Bordet, A. D. Karstensen, D. M. Knowles and C. S. Wiesner, “A New Statistical Criterion For Cleavage Fracture In Steel. Part I: Model Presentation”, Engg. Fract. Mech. 72 (2005) 435-452.

[8] S. R. Bordet, A. D. Karstensen, D. M. Knowles and C. S. Wiesner, “A New Statistical Criterion For Cleavage Fracture In Steel. Part II: Application To An Offshore Structural Steel”, Engg. Fract. Mech. 72 (2005) 453-474.

[9] S. R. Ortner, “The Ductile-To-Brittle Transition In Steels Controlled By Particle Cracking”, Fatigue & Fracture Engineering Mater. Struct., 29 (9/10), 752-769 (2006).

[10] S. G. Roberts, S. J. Noronha, A. J. Wilkinson and P. B. Hirsch, “Modelling The Initiation Of Cleavage Fracture Of Ferritic Steels”, Acta Mater., 50, 1229-1244 (2002).

[11] K. Wallin, “Irradiation Damage Effects On The Fracture Toughness Transition Curve Shape For Reactor Pressure Vessel Steels”, Int. J. Press. Ves. & Piping, 55, 61-79 (1993).

[12] Kurt Thorn, Confocal Microscopy, Lecture, iBioSeminars, [online], URL Address: http://206.241.3.92/lectures/bio-techniques/kurt-thorn.html

[13] S. Lee, S. Kim, B. Hwang, B. S. Lee, C. G. Lee , Effect of carbide distribution on the fracture toughness in the transition temperature region of an SA 508 steel, Acta Material 50, 4755-4762, 2002.

Table 1: Summary of inclusion analyses – per unit area

Number of Inclusion analysed	Total Area [µm^2]	Total Area [mm^2]	Number of Inclusions per µm^2	Number of Inclusions per mm^2	Total surface fraction [%]
2720	327578	0.33	0.0083	8303	0.17

Table 2: Average inclusion measurements

Area [µm2]	Perimeter [µm2]	Width [µm]	Height [µm]	Feret's Diameter [µm]	Nearest Neighbour Distance [µm]	Equivalent "Area" Diameter [µm]	Equivalent "Perimeter Diameter [µm]
0.3±0.1	1.6±0.1	0.5±0.2	0.5±0.2	0.6±0.2	5.6±0.1	0.5±0.2	0.5±0.2

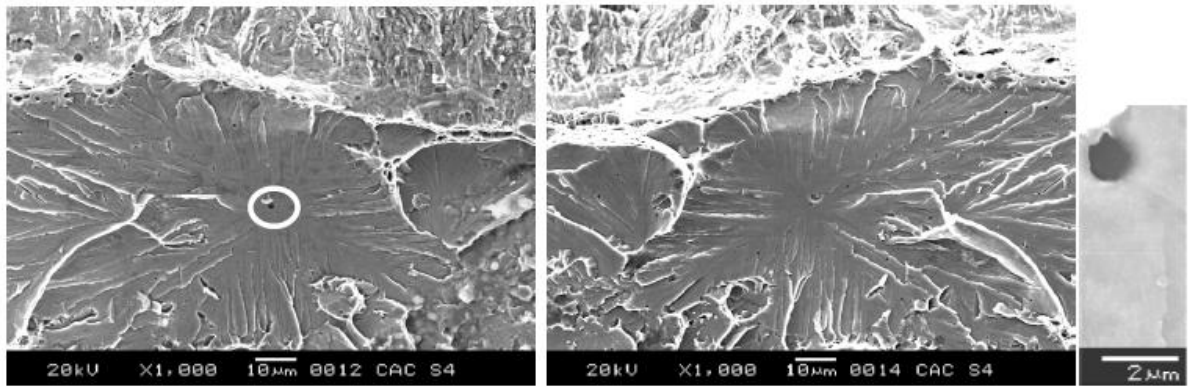

a) b) c)

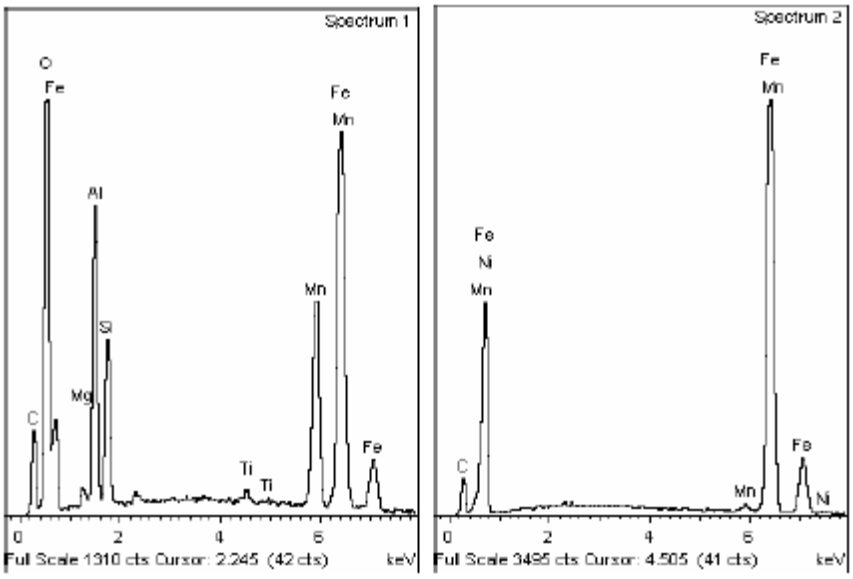

d) e)

Figure 1: a) and b) Images of dominant initiation site from matching halves of sample CAC S4, c) detail of site from (a) with adjusted brightness to show remnants of particle within hole, d) Spectrum from particle remnants, e) spectrum from matrix

Figure 2: Light optical micrograph of the "electropolished" TEM-type specimen of weld P141 CAC S7

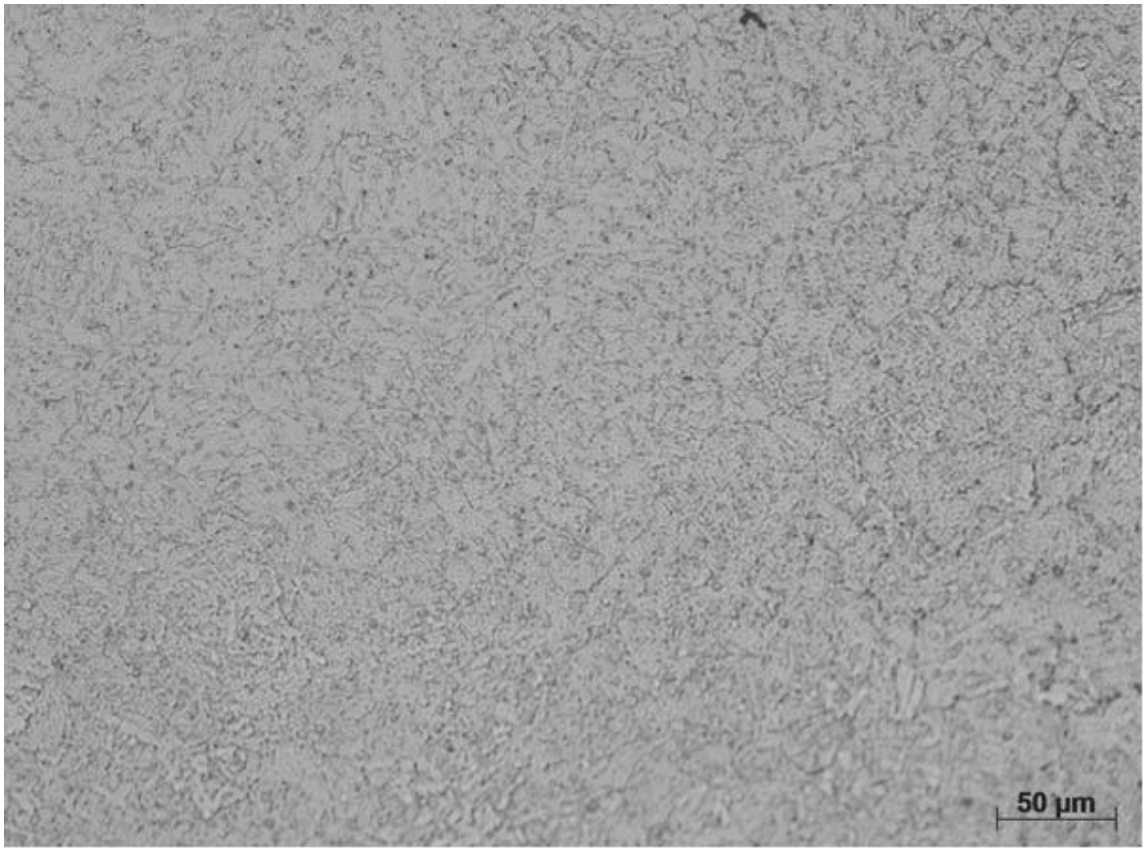

Figure 3: Light optical microscopy of P141 CAC S7

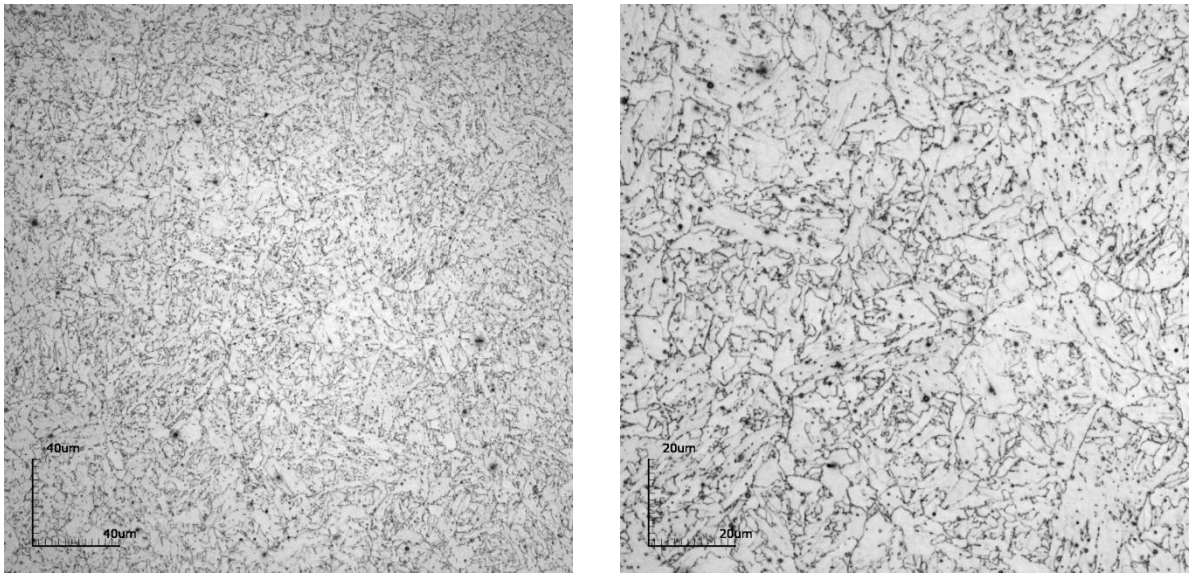

(a) (b)

Figure 4: Light optical micrographs obtained using laser scanning confocal microscopy of electro-etched TEM specimen of P141 CAC S7

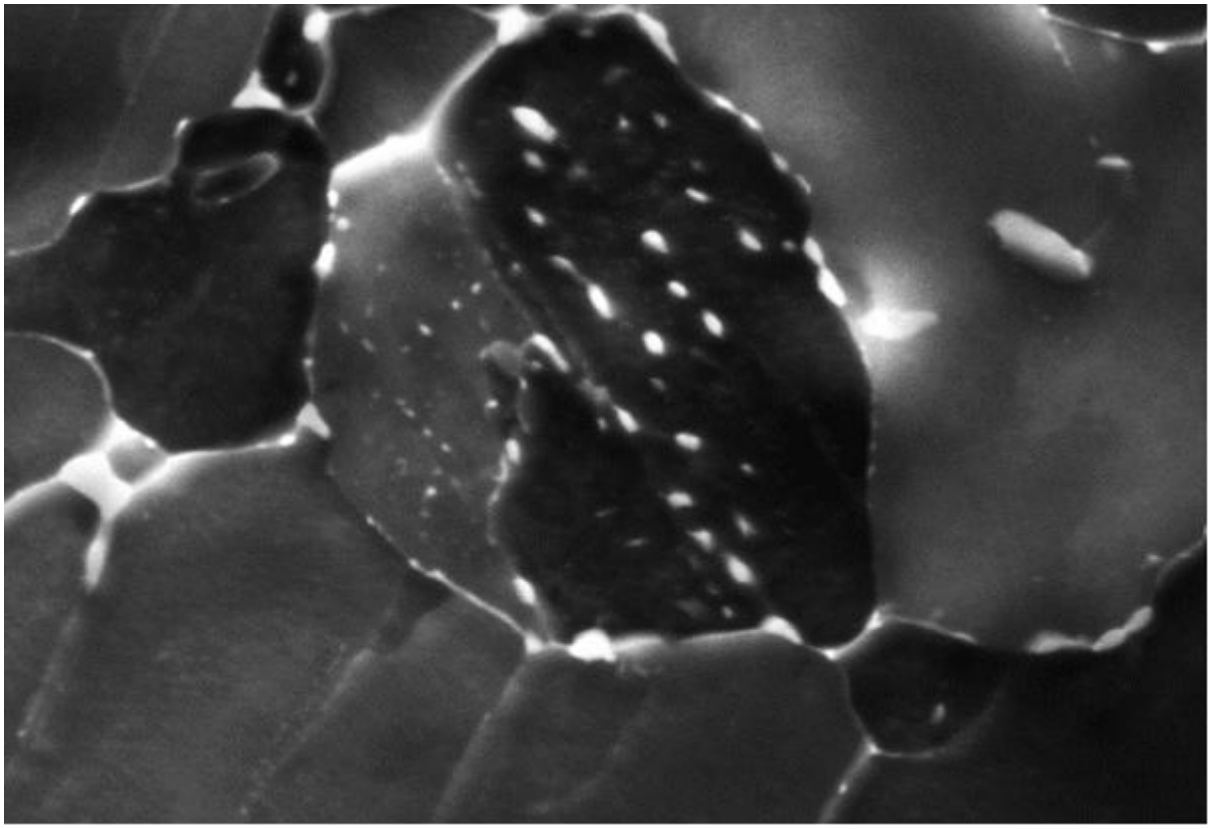

Figure 5: Secondary electron (SE) image of electroetched TEM specimen showing the bainitic microstructure.

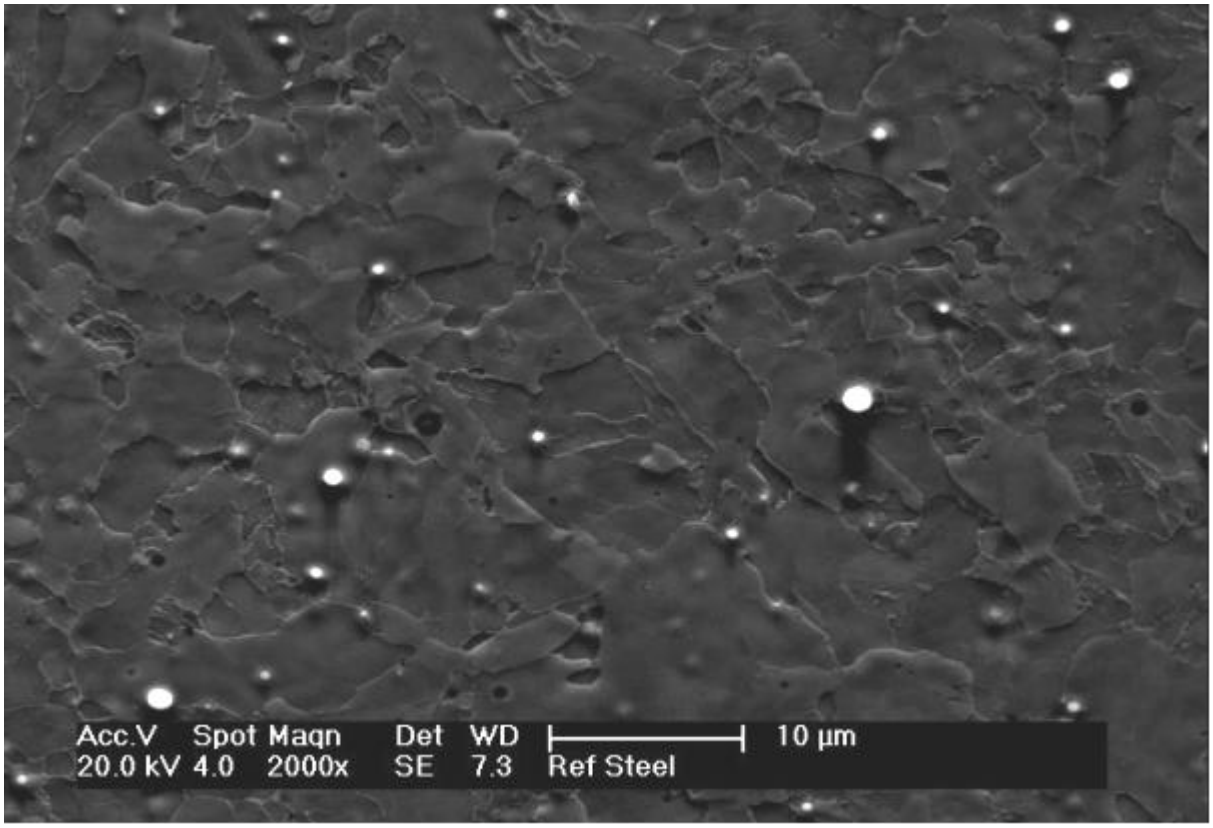

Figure 6: SE image obtained from the "electropolished" TEM-type specimen. Note the ferritic microstructure and the brightly-imaging spheroidal inclusions

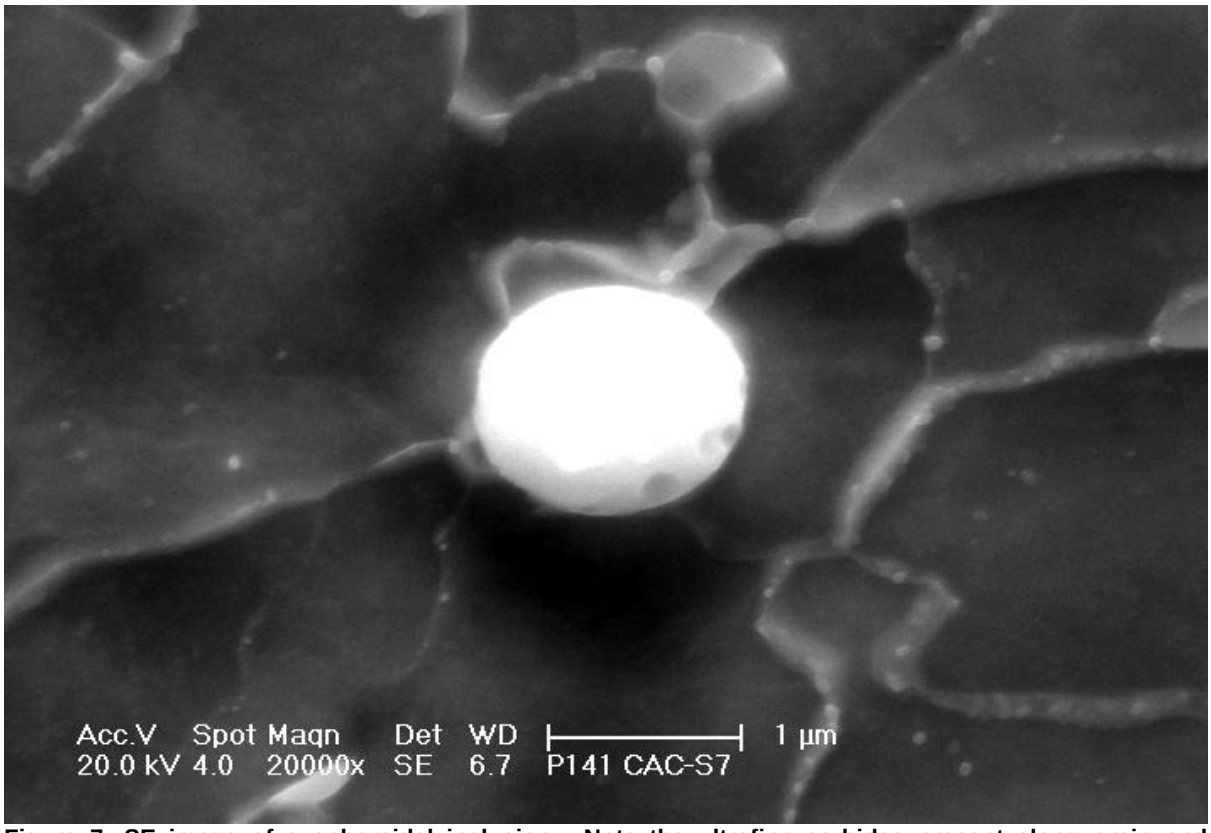

Figure 7: SE image of a spheroidal inclusion. Note the ultrafine carbides present along grain and subgrain boundaries

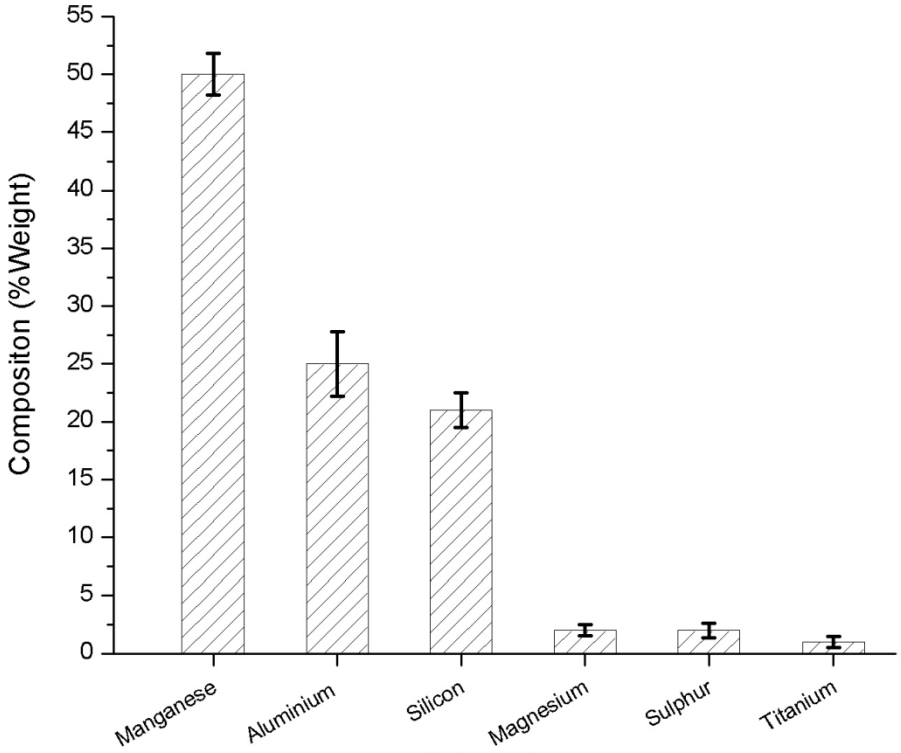

Figure 8: Chemical composition of the inclusions in P141 CAC-S7 weld metal

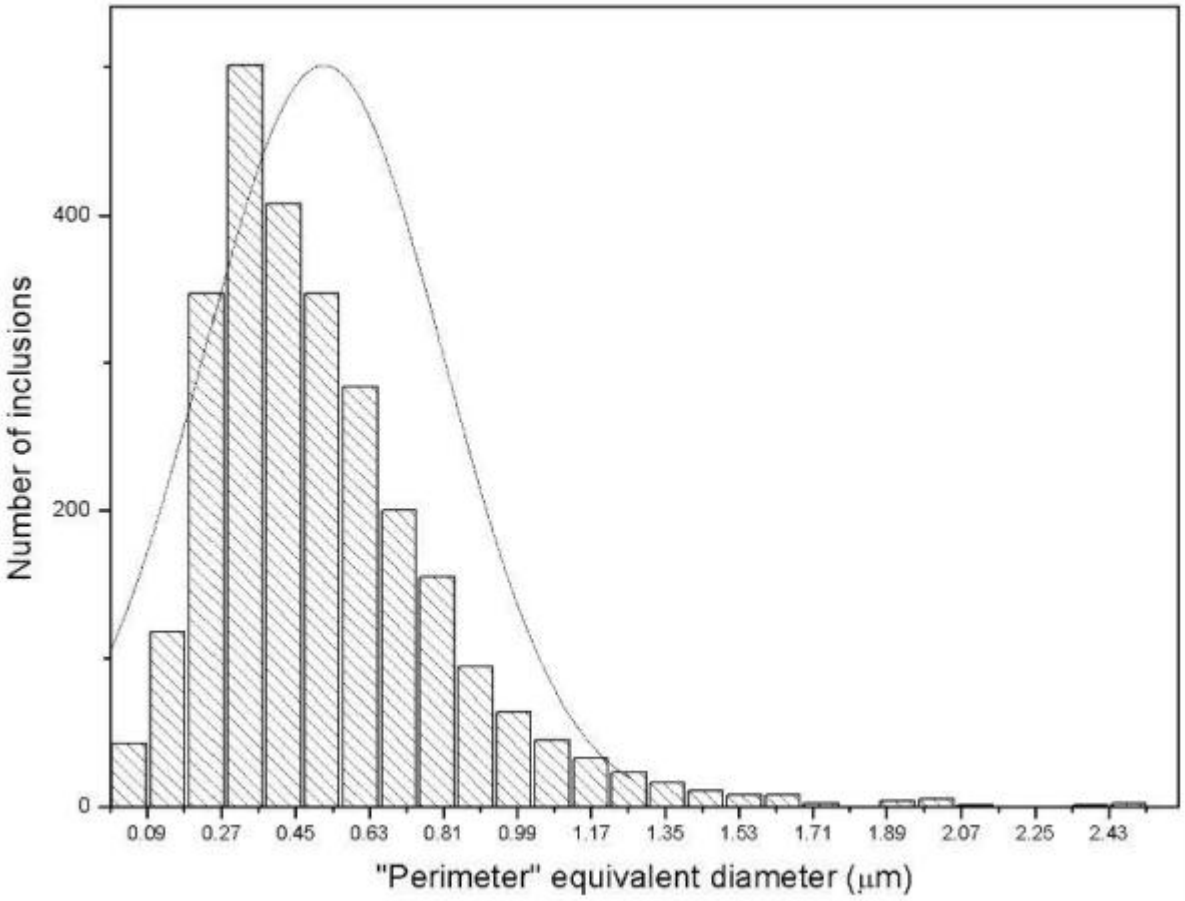

Figure 9: Size distribution of the inclusions: application to the "perimeter" equivalent diameter. Note the difference between the inclusion size distribution and a Gaussian distribution.

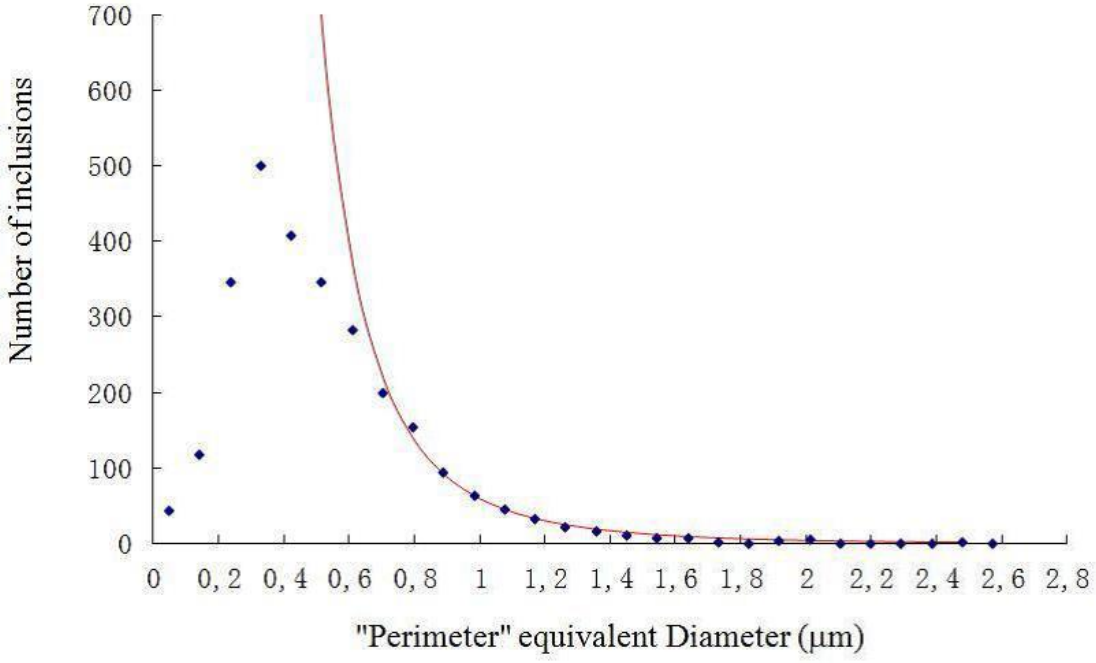

Figure 10: Power law fitting of the experimental data: application to the "perimeter" equivalent diameter

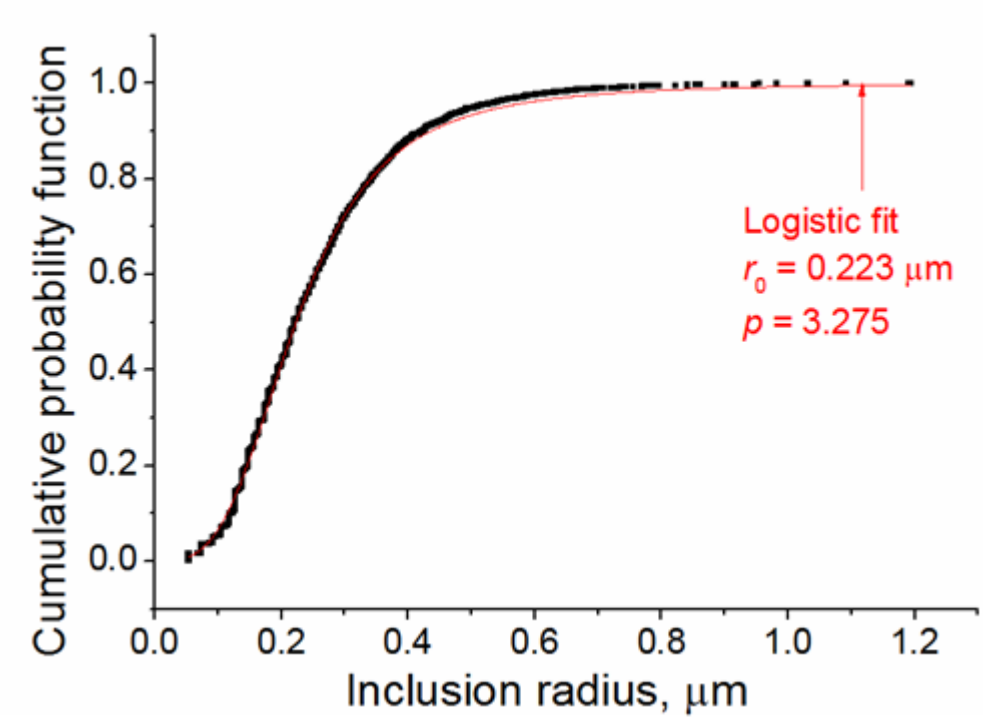

Figure 11: Cumulative probability of inclusion sizes and best fit to data provided by logistic function.